Q. J. R. Meteorol. Soc. (1995), 121, pp. 55–77 551.515.61:551.574.14

Melting and freezing in a mesoscale convective system

By SCOTT A. BRAUN* and ROBERT A. HOUZE Jr
University of Washington, USA

(Received 7 January 1994; revised 31 May 1994)

SUMMARY

Microphysical and thermodynamic fields retrieved from dual-Doppler synthesized winds are used to examine the distribution of melting and freezing rates within a midlatitude squall line with trailing stratiform precipitation. Previously, the effect of the heating/cooling processes associated with the release/consumption of the latent heat of fusion have emphasized the melting layer in the stratiform precipitation region, where the layer is typically marked by a radar bright band. The retrieved fields reveal the melting and freezing in the convective as well as stratiform region. Two-dimensional retrieved fields indicate that the strong melting effect is not confined to the stratiform region, but extends across the entire breadth of the storm. The peak rates of cooling in the stratiform precipitation region are -2 to $-3\,K\,h^{-1}$, in general agreement with previous studies. In contrast, cooling rates in the convective precipitation region reach $-14\,K\,h^{-1}$. The heating by freezing is concentrated in a vertical column associated with the convective updraughts, with peak heating rates of $8\,K\,h^{-1}$ just above the 0 °C level. For the mature stage of the storm, the convective region is found to account for 56% of the total cooling by melting, and 87% of the total heating by freezing within the squall line.

A one-dimensional retrieval model is applied to mean vertical-velocity profiles to retrieve area-mean profiles of the melting and freezing rates. In the convective region, average cooling rates of $-10\,K\,h^{-1}$ are found. The strong cooling by melting is expected to exert a strong influence on the development of convective downdraughts, the cold pool, and the gust front. The heating by freezing occurs through a deep layer, with a peak average heating rate of about $4\,K\,h^{-1}$ just above the 0 °C level. In the stratiform precipitation region, a melting rate of about $-2\,K\,h^{-1}$ produced a near 0 °C isothermal layer approximately 500 m deep, similar to isothermal layers observed in stratiform precipitation areas associated with fronts.

1. INTRODUCTION

Mesoscale convective systems (MCSs) at midlatitudes and in the tropics frequently contain large regions of stratiform precipitation. Within these stratiform regions, radar bright bands are often seen near the 0 °C level. The regions of enhanced reflectivity associated with bright bands in the stratiform precipitation regions of MCSs are frequently organized in elongated zones to the rear of, and parallel to, a line of strong convection. These *secondary* bands can be located parallel to the convective line all along its length (symmetric organization, Houze *et al.* 1990) or they can be contained largely towards one end of the squall line (asymmetric organization). Bright bands are generally attributed to a rapid enhancement of particle size just above the melting layer as a result of aggregation, and to changes within the melting layer of the dielectric properties, size, and fall speeds of the melting particles (Houze 1993, p. 201).

Leary and Houze (1979) have shown that the cooling rate associated with melting in the stratiform regions of tropical MCSs can be as strong as the cooling associated with evaporation. Although the contribution to the total atmospheric cooling by melting produced in the stratiform region is generally small compared with that for evaporation, the cooling from melting is concentrated within a shallow layer, thus enabling it to have a substantial impact on the temperatures within the system. Stewart (1984) has shown that cooling by melting associated with frontal clouds can produce near 0 °C isothermal layers as deep as 1 km. Similar isothermal layers have been noted within the stratiform regions of MCSs (Willis and Heymsfield 1989; Zhang and Gao 1989). Atlas *et al.* (1969)

* Corresponding author: Department of Atmospheric Sciences, AK-40, University of Washington, Seattle, WA 98195, USA.

found small mesoscale wind perturbations within the melting layer of a frontal cloud, and attributed these wind perturbations to perturbations in the pressure field produced by melting. Using a two-dimensional (2D) hydrostatic model, Szeto *et al.* (1988a, b) verified that the cooling by melting within stratiform precipitation can produce significant mesoscale circulations, particularly when combined with the cooling associated with evaporation (Szeto *et al.* 1988b).

While melting has been discussed previously in reference to the stratiform precipitation regions of MCSs, the melting within the convective region has been largely neglected. For example, in heat-budget studies of squall lines with trailing stratiform precipitation in the tropics (Houze 1982; Chong and Hauser 1990), cooling by melting has been considered only within the stratiform precipitation region. The reason the melting in the convective region has been neglected in the past is probably that it does not produce a readily identified signature in a vertical cross-section of radar reflectivity. Recent studies using dual-polarization radar have, however, demonstrated the melting of ice-phase precipitation in both stratiform (Bader *et al.* 1987) and convective precipitation (Bringi *et al.* 1986a, b; Illingworth *et al.* 1987; Wakimoto and Bringi 1988; Vivekanandan *et al.* 1990; Fulton and Heymsfield 1991; Meischner *et al.* 1991; Yuter and Houze 1994.

Meischner *et al.* (1991) present an example of the differential reflectivity field associated with a squall line with trailing stratiform precipitation. Their results for a squall line in Germany clearly reveal the occurrence of a melting layer within the convective region of the squall line. However, they did not provide quantitative information on the melting rates within the convective and stratiform regions of the squall line. Thus, questions about the rates of cooling by melting in the convective region remain to be addressed. How strong is the cooling by melting in the convective region How does it compare with that in the stratiform precipitation region? How much does the cooling by melting in the convective region contribute to the total cooling by melting within the MCS?

Even less is known about the heating produced by freezing and its vertical distribution within convection. Studies by Waldvogel *et al.* (1987), Fulton and Heymsfield (1991), Meischner *et al.* (1991), and Yuter and Houze (1994) indicate substantial amounts of precipitating ice immediately above the freezing level, suggesting that glaciation occurs fairly rapidly as supercooled drops are carried above the freezing level within the convective updraughts. Koenig (1963) and Hallett *et al.* (1978) have shown that significant glaciation can occur within 2–5 min. However, the heating associated with freezing and its vertical distribution have yet to be quantified.

In this study we use the thermodynamic and microphysical retrieval results of Braun and Houze (1994, hereafter referred to as BH1) to quantify and map the melting and freezing rates within the midlatitude squall line which occurred on 10–11 June 1985 in Oklahoma and Kansas during PRE-STORM (Preliminary Regional Experiment for the STormscale Operational and Research Meteorology) (Cunning 1986). Furthermore, we use the one-dimensional (1D) microphysical retrieval methodology developed by Braun and Houze (1995, hereafter referred to as BH2) to estimate vertical profiles of the melting and freezing rates from vertical profiles of mean vertical velocity. We will show that for the 10–11 June squall line, the area-averaged cooling by melting within the convective and stratiform precipitation regions contributed nearly equally to the total cooling by melting within the squall line, and that the melting rates within the convective region were very intense. Further, we will show that the heating by freezing is contained almost entirely within the convective region, with the peak heating rate occurring immediately above the freezing level.

2. DATA

The 10–11 June 1985 squall line has been extensively examined in previous studies (Smull and Houze 1987; Rutledge *et al.* 1988a; Johnson and Hamilton 1988; Willis and Heymsfield 1989; Zhang and Gao 1989; Biggerstaff and Houze 1991a, b, 1993; BH1; BH2). Rutledge *et al.* (1988a) and Biggerstaff and Houze (1991a, b, 1993) describe the radar characteristics, the processing of the dual-Doppler radar data, the reflectivity structure, and the kinematics of the squall line.

Retrieval of thermodynamic and microphysical variables from a composite of dual-Doppler synthesized wind and reflectivity data produced by Biggerstaff and Houze (1993) was performed by BH1. The retrieval methodology was applied to a mean cross-section of reflectivity and velocity (Fig. 1), obtained by averaging in the along-line direction over

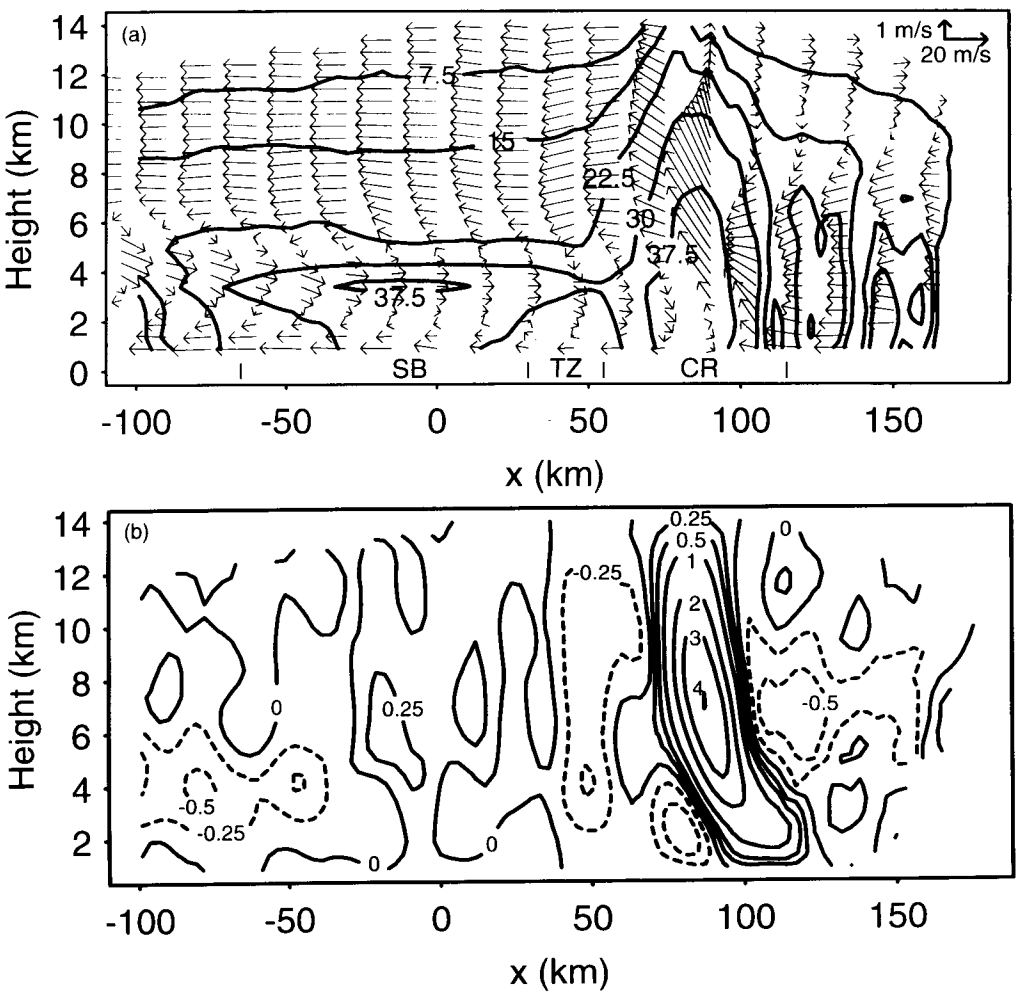

Figure 1. (a) Along-line averaged radar reflectivity (contoured every 7.5 dBZ) and storm-relative wind vectors in the plane of the cross-section. The arrows in the upper right corner represent the arrow scales corresponding to 1 m s^{-1} for the vertical velocity and 20 m s^{-1} for the horizontal velocity. The approximate positions of the secondary band (SB), transition zone (TZ), and convective region (CR) are indicated along the bottom of the figure. (b) Along-line averaged vertical velocity (m s^{-1}). Positive values are indicated by the solid lines and negative values by the dashed lines.

a 60 km wide strip. Good agreement was found between the observed radar-reflectivity structure and the fields of retrieved precipitation (Fig. 2) and reflectivity (Fig. 7 of BH1). In particular, the retrieval was able to reproduce the secondary maximum of precipitation associated with the secondary band ($x = -70$ to 30 km), as well as the precipitation minimum within the transition zone ($x \approx 30$ to 55 km). BH1 determined that the primary processes accounting for the observed radar-reflectivity structure in the stratiform region were: (1) the substantial growth by vapour deposition of precipitating ice particles generated in, and detrained from, convective cells and falling out through the region of mesoscale ascent in the stratiform region; (2) the strong aggregation of ice particles above the bright band in the region of the secondary band, which affected the size distribution of raindrops below the bright band such that the reflectivity was enhanced; and (3) the suppression of growth in the mid-level descent just behind the convective region, which slightly enhanced the minimum of radar reflectivity in that zone.

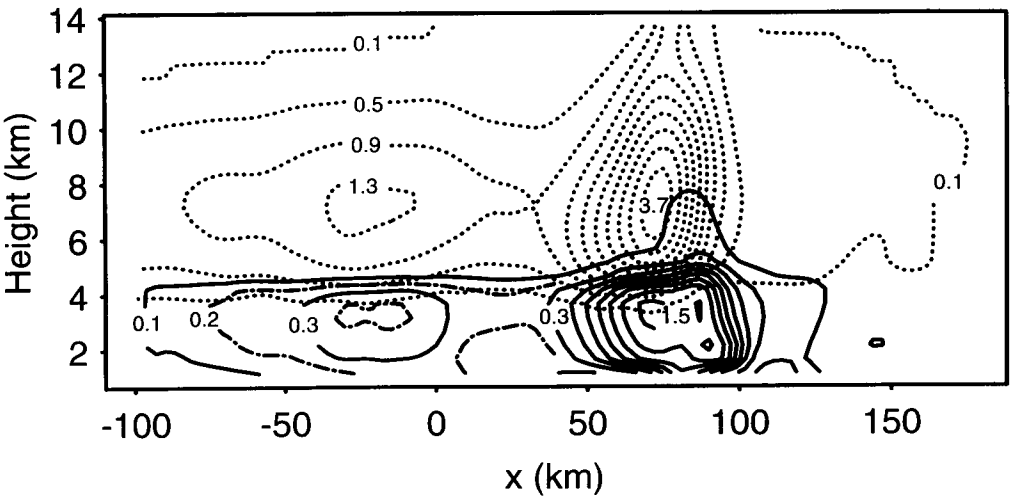

Figure 2. Mixing ratios of rain (solid) and precipitating ice (dotted). Contours are drawn every 0.2 g kg^{-1} for rain and every 0.4 g kg^{-1} for precipitating ice, starting at 0.1 g kg^{-1}. For rain, additional contours (dot-dashed) are drawn at 0.2 and 0.4 g kg^{-1}.

In section 3 we use the retrieval results of BH1 to examine the 2D distribution of melting and freezing rates within the squall line. In section 4 we use dual-Doppler synthesized wind and radar-reflectivity data from the east dual-Doppler lobe (see Fig. 1 of Biggerstaff and Houze (1991a)) at 0139 and 0209 UTC 11 June 1985 as input to the 1D retrieval calculations in the convective region. For the stratiform region we use the 0345 UTC average vertical-velocity profile from the CP-4 radar presented in Fig. 11 of Rutledge *et al.* (1988a). The stratiform region calculations also make use of low-level soundings taken within the stratiform precipitation region between 0300 and 0600 UTC 11 June. Those soundings generally terminated between 3.5 and 4.0 km (near the melting level) since they were unable to penetrate through the anvil cloud.

3. Two-dimensional retrieval results

The distributions of the cooling rate associated with melting and the heating rate from freezing, determined from the retrieval results of BH1, are shown in Fig. 3. The

corresponding fields of the rain and precipitating-ice mixing ratios are in Fig. 2. The melting rates in the convective region reach a maximum of $-14\,\mathrm{K\,h^{-1}}$ just behind the mean convective updraught and above the mean convective downdraught ($x = 70$ km, $z = 4$ km). Melting rates in the stratiform region generally range from -2 to $-3\,\mathrm{K\,h^{-1}}$, consistent with the values determined from radar-reflectivity profiles in tropical convective systems by Leary and Houze (1979).

While melting occurs within a rather shallow but horizontally extensive layer, the freezing of rain and cloud-water occurs almost entirely within a deep vertical column associated with the convective updraught. Freezing commences immediately above the 0 °C level and reaches a peak in heating of $8.7\,\mathrm{K\,h^{-1}}$ near $x = 87$ km and $z = 5.1$ km. The heating is largely produced by the collection of rain by precipitating ice between 4.6 and 7.6 km, and by the collection of cloud-water by precipitating ice between 5.1 and 10.6 km. Heating rates associated with the freezing of small quantities of cloud-water (by riming) in the stratiform region are less than $1\,\mathrm{K\,h^{-1}}$.

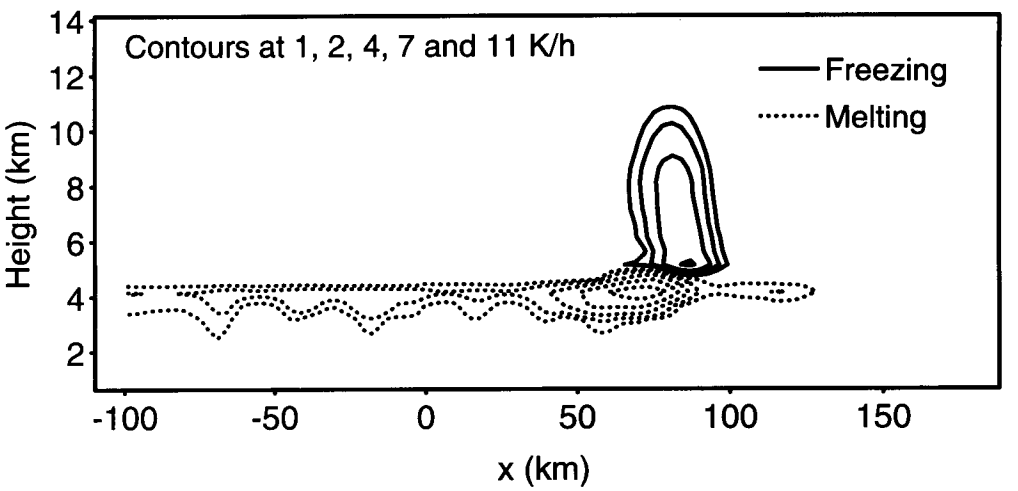

Figure 3. Melting and freezing rates determined from the microphysical retrieval results of BH1.

Average heating and cooling rates for the convective and stratiform precipitation regions are shown in Fig. 4. The convective region profile (Fig. 4(a)) was obtained by averaging from $x = 40$ to 105 km, while the stratiform region profile (Fig. 4(b)) was determined by averaging over $x = -100$ to 40 km. These boundaries were determined subjectively from the fields of vertical velocity and precipitation mixing ratio, and should be sufficient for the present discussion. The cooling in the convective region reaches a peak value of $-7.0\,\mathrm{K\,h^{-1}}$ at 4.1 km, while the cooling in the stratiform region has a maximum rate of $-2.6\,\mathrm{K\,h^{-1}}$ at the same altitude. In both profiles the melting is spread over relatively deep layers as a result of the limited vertical resolution of the composite data set (500 m), which prevents the relaxation method used in the retrieval from completely removing all of the precipitating ice at lower levels. The limited vertical resolution also causes the intense portions of the melting layers in the convective and stratiform regions to be of similar depth (Figs. 3 and 4). The heating by freezing occurs almost entirely within the convective region and reaches a peak value of $2.2\,\mathrm{K\,h^{-1}}$ at 5.1 km.

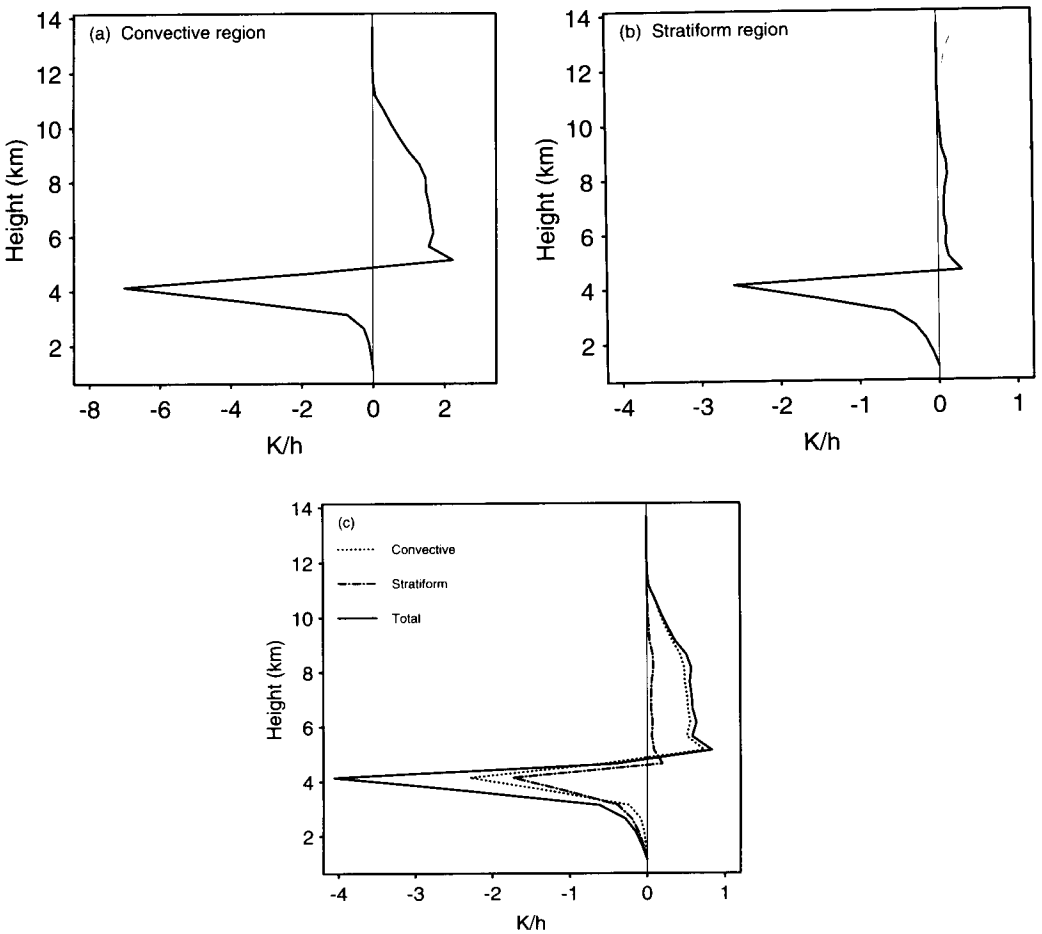

Figure 4. Average heating and cooling rates associated with freezing and melting, respectively, for (a) the convective region (x = 40 to 105 km), (b) the stratiform region (x = −100 to 40 km), and (c) the total storm (x = −100 to 105 km). In (c), the area-weighted average rates for the convective and stratiform regions are shown. Freezing rates are indicated by positive values, melting rates by negative values since freezing (melting) always produces positive (negative) heating rates. Therefore, the single line shows both freezing and melting rates.

The contributions of the heating and cooling in the convective and stratiform regions to the total heating and cooling (taken as the average over x = −100 to 105 km) are shown in Fig. 4(c). The convective and stratiform components were obtained by multiplying the heating/cooling rates in Figs. 4(a) and 4(b) by the respective fractional areas of the two regions (i.e. the fraction of the total area from x = −100 to 105 km which the convective and stratiform regions cover). From Fig. 4(c) it can be seen that the convective region contributes slightly more than half to the total cooling by melting despite the fact that the stratiform region occupies an area more than twice as large as the convective region. As noted above, the heating by freezing is largely confined to the convective region.

Tao *et al.* (1993) used a nonhydrostatic cloud model to simulate the 10–11 June squall line and derive estimates of the heat budget. They found that when averaged over the lifetime of the squall line, melting in the convective region contributed to about 42% of the total melting in the squall line, while freezing in the convective region accounted for 66% of the total freezing. When the freezing and melting rates in Fig. 3 are summed

separately over the convective and stratiform precipitation regions, we find for the mature stage of the squall line that the melting and freezing in the convective region account for 56% and 87%, respectively, of the total melting and freezing. The smaller contribution to the total melting and freezing by the convective region found in Tao *et al.* (1993) has several possible explanations. First, it might result from averaging over the lifetime of the squall line in their study, since during the decaying stage of the system melting in the stratiform precipitation region is greater than that in the convective region, and freezing in the convective region is substantially diminished. Second, differences in the microphysical parametrization schemes may also lead to differences in the microphysical variables and heating and cooling rates. Finally, differences in the contributions of the convective and stratiform regions may result from differences in how these regions are defined when averaging. In our analysis we simply specified the division between the two regions at $x = 40$ km, whereas Tao *et al.* (1993) based their separation of the convective and stratiform components on criteria applied to the rainfall rate, vertical velocity, and cloud-water mixing ratio. Tao *et al.* (1993) also simulated a tropical squall line, for which they found that the convective region produced only about 14% of the total melting. Apparently, either less ice was produced because of weaker updraughts or much of the ice generated within the convective region was advected rearward into the stratiform region before melting. If this result is typical of tropical systems, then the exclusion of melting in the convective region from the heat-budget studies of Houze (1982) and Chong and Hauser (1990) was justified.

4. Melting-rate and freezing-rate profiles for the convective and stratiform regions

Heat budgets for regions containing convective clouds are often determined from large-scale measurements obtained by rawinsonde (Yanai *et al.* 1973; Kuo and Anthes 1984; Gallus and Johnson 1991; Lin and Johnson 1994). While these data are useful for estimating the total heating in a large-scale area, resolution limits make the separation of the total heating into its convective and stratiform components very difficult. This study is part of an effort to estimate the heat budget of the 10–11 June 1985 squall line from dual-Doppler radar data, which have the resolution necessary to distinguish the convective and stratiform components of the total heating. The heat budget will be estimated from mean vertical-velocity data in a manner following Houze (1982). As shown in section 3, melting and freezing are important processes within both the convective and stratiform precipitation regions. Therefore, calculations of latent heating from vertical-velocity profiles should include these processes. In the stratiform region, reflectivity profiles can be used to estimate the melting rate (Leary and Houze 1979); however, this method cannot be applied to the convective region. Furthermore, estimates of the freezing rates are also needed. In this section we use the 1D microphysical retrieval of BH2, which allows for retrievals of vertical profiles of the microphysical variables and the freezing and melting rates from vertical profiles of area-mean vertical velocity. This method obtains bulk estimates of the vertical profiles of hydrometeors and melting and freezing rates without performing detailed 2D or three-dimensional (3D) retrievals. In section 4(a) we verify the 1D results for the convective region by comparing the melting and freezing rates from the 1D model with average values from the 2D retrieval fields. Then, in sections 4(b) and 4(c) we apply the method to vertical profiles of vertical velocity for the convective and stratiform regions of the 10–11 June storm.

(a) *Verification*

BH2 applied their 1D retrieval technique to the average vertical velocity determined in the convective region from the composite radar data of Biggerstaff and Houze (1993) (see Fig. 7 of BH2). They showed that the profiles of hydrometeor mixing ratios obtained from the 1D model compared well with the profiles of the average mixing ratios determined from the 2D retrieval of BH1. However, if we are to use the 1D retrieval methodology to estimate melting and freezing rates, then we must also show that the melting and freezing rates determined from the 1D model are in good agreement with the average rates from the 2D analysis of BH1. This verification is given below.

The melting and freezing rates for the 1D results (corresponding to the mixing-ratio profiles in Fig. 9 of BH2) and the convective region average rates from Fig. 4(a) are shown in Fig. 5. The cooling rates associated with melting are reproduced almost exactly. The 1D retrieval slightly underestimates the heating rates associated with freezing, but this difference is relatively small. It thus appears that the 1D model provides good estimates of the melting and freezing rates within the convective region.

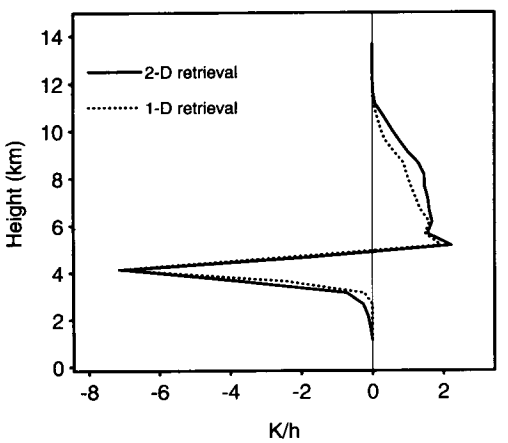

Figure 5. Retrieved vertical profiles of the melting and freezing rates from the two-dimensional retrieval and the one-dimensional retrieval.

(b) *Convective region*

For the convective region we determined average vertical velocities for the convective region of the 10–11 June squall line from dual-Doppler syntheses of the 3D winds in the east dual-Doppler lobe. Figure 6 shows the low-level radar-reflectivity fields at 0139 UTC and 0209 UTC. At 0139 UTC (Fig. 6(a)) the dual-Doppler domain includes a roughly 95 km long segment of the northern portion of the squall line. At 0209 UTC (Fig. 6(b)) a segment about 110 km in length is covered. The polygons in Fig. 6 indicate the areas over which the vertical-velocity data were averaged. These polygons were determined subjectively by examining horizontal and vertical cross-sections through the storm, and roughly enclosing regions of high reflectivity and strong reflectivity gradient. We attempted to exclude regions of missing data from the averaging domains.

In Fig. 7 we show the profiles of mean vertical velocity at 0139 UTC (solid) and 0209 UTC (dot-dashed). The mean velocity at 0139 UTC shows a maximum value of 2.0 m s^{-1} near 8.5 km altitude, while at 0209 UTC the maximum velocity is 2.4 m s^{-1} at approximately 8 km. These mean velocities are more than double the convective region

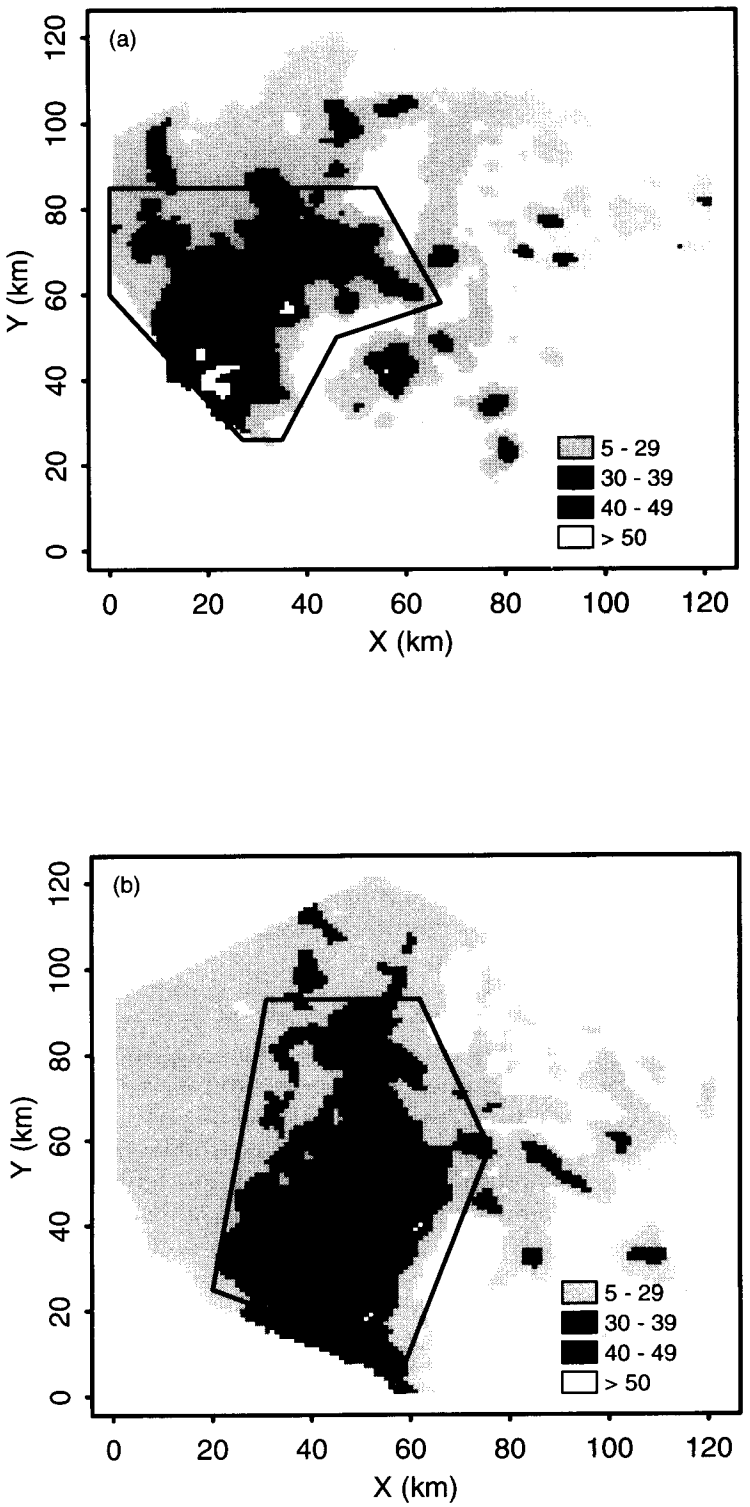

Figure 6. Radar reflectivity (dBZ) at 1.9 km from the east dual-Doppler lobes at (a) 0139 UTC and (b) 0209 UTC 11 June 1985. The polygons enclose the regions from which the average vertical velocities are obtained.

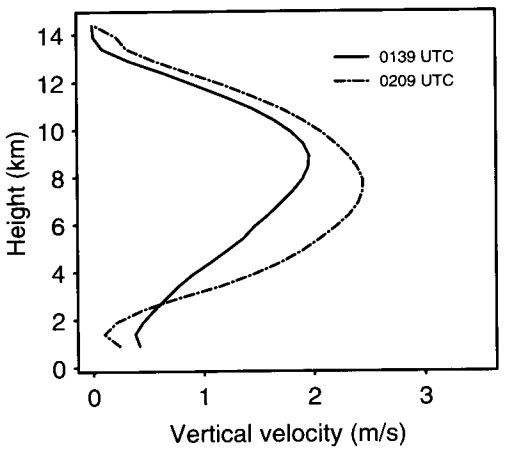

Figure 7. Average vertical-velocity profiles for 0139 UTC and 0209 UTC 11 June 1985 obtained from the areas indicated in Fig. 6.

average values from the radar composite (Fig. 7 of BH2). The weakness of the composite profile results partially from the lower resolution of the composite fields (3 km versus 1 km). However, it is also apparent that the strength of the vertical motions in the composite is weaker as a consequence of the averaging and filtering that was applied to the horizontal wind fields when constructing the composite velocities (see Biggerstaff and Houze 1993; BH1). The differences in vertical velocity between the profiles at 0139 and 0209 UTC may reflect changes of the vertical velocity with time such that th assumption of stationary conditions in the microphysical retrieval is a limitation of the retrieval methodology (BH2). However, the differences may also be attributed to the difference in the location of the averaging domains along the line; i.e. the vertical velocities at the northern tip of the line may have been weaker than the velocities within the line away from the ends, where the precipitation rates were observed to be more intense (see Rutledge *et al.* 1988a, Fig. 3).

Mixing ratios and melting and freezing rates for the vertical-velocity profiles at 0139 and 0209 UTC are shown in Figs. 8 and 9 respectively. At 0139 UTC (Fig. 8(a)), the rain mixing ratios reach 1.4 g kg^{-1} and the precipitating-ice mixing ratios exceed 3 g kg^{-1}. The corresponding melting and freezing rates (Fig. 9, solid line) show peak cooling by melting of -9.9 K h^{-1} at 4.1 km and maximum heating by freezing of 4.0 K h^{-1} at 5.1 km. At 0209 UTC (Fig. 8(b)) the larger mean vertical velocities produce mixing ratios of rain of about 1.6 g kg^{-1} and of precipitating ice of 4.6 g kg^{-1}. In Fig. 9 (dotted line) the cooling rate by melting shows a maximum of -10.9 K h^{-1} at 4.1 km and maximum heating by freezing of 5.3 K h^{-1} at 5.1 km. The stronger freezing rate at 0209 UTC is a consequence of the stronger mean vertical velocities (compared with 0139 UTC), which produce slightly greater rain mixing ratios above the freezing level.

The intense melting in the convective region indicates that melting probably played a substantial role in the thermodynamics of this part of the storm by decreasing the potential temperature and equivalent potential temperature of the air parcels descending within the convective downdraughts. The increase in negative thermal buoyancy can drive strong downdraughts, as shown by Srivastava (1987) and Proctor (1988). Knupp (1987, 1988) found that melting contributed more than 60% to the total cooling along some downdraught parcel trajectories in a High Plains thunderstorm. Therefore, in some cases, the cooling by melting can be instrumental in forcing convective downdraughts.

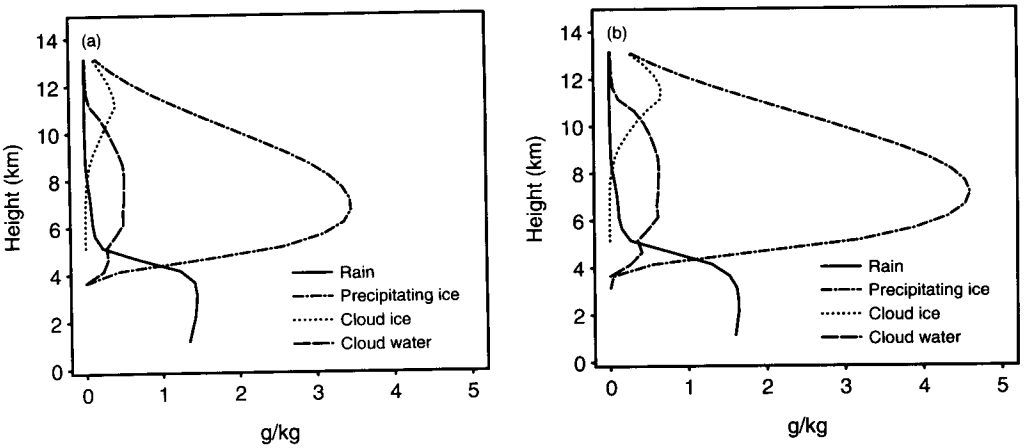

Figure 8. Hydrometeor mixing-ratio profiles for (a) 0139 UTC and (b) 0209 UTC 11 June 1985.

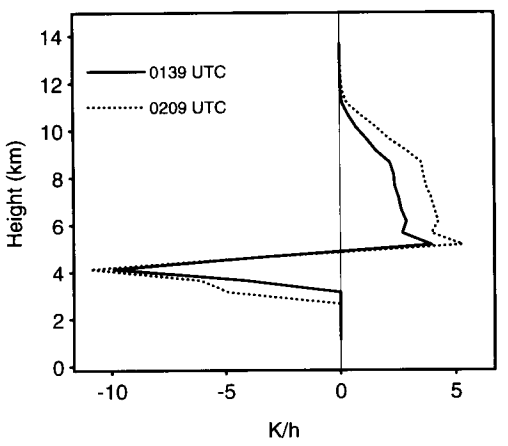

Figure 9. Profiles of melting and freezing rate for 0139 UTC and 0209 UTC 11 June 1985.

The location of the mean convective downdraught in Fig. 1(b) directly beneath the region of strongest cooling by melting (Fig. 3) suggests that melting substantially influenced the strength of the convective downdraughts in the 10–11 June squall line. The strong cooling by melting in the convective region is thus an additional mechanism, along with evaporation, for the intensification of the surface cold pool and gust front.

In their investigation of a squall line in Germany, Meischner *et al.* (1991) identified shallow feeder cells which formed near the gust front in advance of the main convective line. These cells were characterized by low radar reflectivity and high differential reflectivity (Z_{DR}), leading Meischner *et al.* to conclude that the cells contained low concentrations of large raindrops, sometimes extending above the freezing level. Z_{DR} measurements within some of the feeder clouds clearly indicated ice immediately above the freezing level, implying that glaciation occurred rapidly in these cells. The feeder cells were then observed to merge with the main convective line. Z_{DR} measurements in the convective line also indicated ice immediately above the freezing level as well as small melting hail or graupel within a 1.5–2 km deep layer below the melting level. Thus, the multi-

parameter radar analysis of Meischner *et al.* (1991) is consistent with our finding that the freezing begins immediately above the freezing level, and that significant cooling by melting can occur within the convective region. The retrieval results presented above further indicate that the heating by freezing can extend vertically to higher levels (up to 10 km) as a result of the accretion of cloud water by the precipitating ice particles within the deep convective updraughts.

Convective parametrizations often do not include the effects of ice. One exception is the parametrization scheme of Fritsch and Chappell (1980). For the heating associated with freezing, they assume that all of the freezing occurs at a single level (they used the −25 °C level), at which point the equivalent potential temperature (θ_e) of the parcel increases. In contrast, our results indicate that the freezing occurs through a deep layer in the convective region, with the peak heating just above the freezing level. The θ_e of the parcel evidently begins to increase immediately above the freezing level so that the parcel may then attain a slightly stronger vertical velocity as a result of the increased buoyancy. It is uncertain whether the inclusion of a profile of heating by freezing similar to those shown in Fig. 9 would produce significant changes in simulations using the Fritsch–Chappell scheme since the total heating is generally dominated by condensation.

(*c*) *Stratiform region*

For the stratiform region we estimate the cooling by melting by the method outlined in Leary and Houze (1979), as well as by applying the 1D retrieval model to a mean stratiform region vertical-velocity profile. We use the reflectivity, fall speed, and vertical velocity obtained from the CP-4 radar at 0345 UTC by Rutledge *et al.* (1988a)* using the Extended Velocity Azimuth Display (EVAD) method (Srivastava *et al.* 1986). The CP-4 profiles of reflectivity and fall speed are shown in Fig. 10(a) and the vertical velocit is shown in Fig. 10(b). The melting level, shown at 4.3 km in Fig. 10(a), was estimated

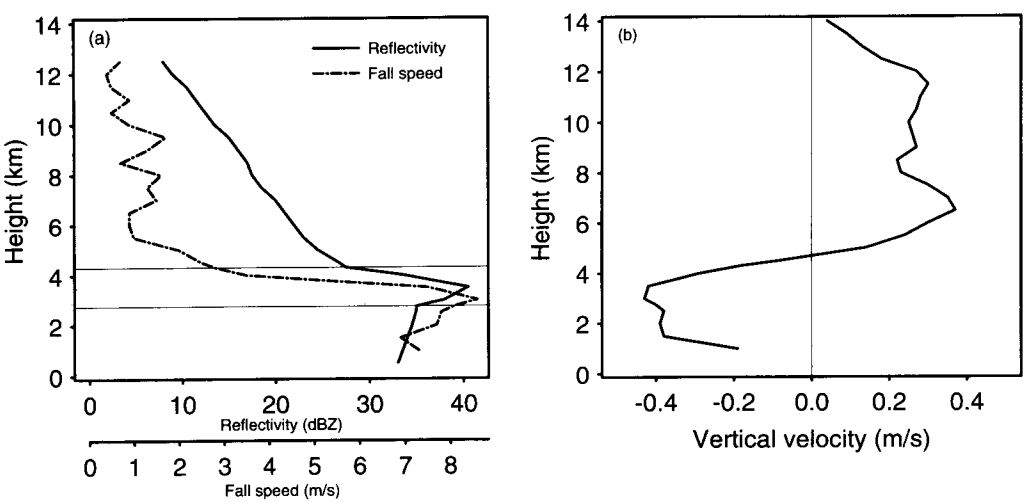

Figure 10. (a) Radar reflectivity and fall speed, and (b) vertical velocity from the CP-4 radar at 0345 UTC 11 June 1985 (adapted from Rutledge *et al.* (1988a)). The horizontal lines in (a) indicate the estimated top and bottom of the melting layer.

* We use the Rutledge *et al.* (1988a) profile since the vertical-velocity and terminal fall-speed estimates from the EVAD analysis are expected to be more accurate than the dual-Doppler synthesized motions within the stratiform region.

from a time–height cross-section of fall speed in Rutledge *et al.* (1988a, see their Fig. 14) by assuming that the melting level (top of the melting layer) was located at the top of the layer characterized by large vertical gradients of fall speed.

The reflectivity profile shows a strong peak of 40 dBZ just below the melting level associated with the bright band in the stratiform region of the squall line. Fall speeds above 5 km are about 1.0 to 1.5 m s^{-1}. Below the melting level the fall speeds* reach 8.6 m s^{-1}, decreasing to 7 m s^{-1} near the surface. BH1 suggested that particle growth by deposition and aggregation above the melting level in the stratiform region led to the production of large aggregates just above the radar bright band. The reflectivity and fall-speed profiles below the bright band suggest that large raindrops produced by the melting of the large aggregates subsequently broke up as they fell, resulting in the decreasing reflectivity and fall speeds at lower levels. The vertical-velocity profile (Fig. 10(b)) is typical of stratiform region vertical motions (Houze 1989), with ascent (0.2 to 0.4 m s^{-1}) above 4.5 km and descent (~0.4 m s^{-1}) below this level.

Following Leary and Houze (1979), we obtain two estimates of the melting rate from

$$\frac{\Delta T}{\Delta t} = \frac{V_p L_f q_p}{c_p \Delta z} \tag{1}$$

$$\frac{\Delta T}{\Delta t} = \frac{V_r L_f q_r}{c_p \Delta z} \tag{2}$$

where q_r, q_p, V_r, and V_p are the mixing ratios and fall velocities of rain and precipitating ice, respectively, L_f is the latent heat of fusion, c_p is the specific heat at constant pressure, Δz is the thickness of the melting layer, T is temperature, and t is time. Equation (1) is applied at the top of the melting layer and (2) at the bottom of the layer. Leary and Houze (1979) assumed fall speeds of 1.5 and 6.0 m s^{-1} for precipitating ice and rain, respectively. Here, we use the EVAD estimated fall speeds (Fig. 10(a)). The rain and precipitating-ice mixing ratios, q_r and q_p are estimated from the equivalent radar-reflectivity factor, Z_e for rain and Z_i for ice, following Leary and Houze (1979)

$$\rho q_p = 8.0 \times 10^{-3} Z_i^{0.61} \tag{3}$$

$$\rho q_r = 5.5 \times 10^{-4} Z_e^{0.80} \tag{4}$$

where ρ is the density of air. The bottom of the melting layer is taken to be the height at which the curvature of the reflectivity profile changes abruptly, as in Leary and Houze (1979). This level is indicated in Fig. 10(a) at 2.8 km.

Table 1 shows the value of each of the variables in Eqs. (1)–(4) and the estimated cooling rates. There is good agreement between the cooling rates determined at the top (Eqs. (1) and (3)) and the bottom (Eqs. (2) and (4)) of the melting layer. The average cooling rate of about −2.6 K h^{-1} is somewhat less than the average value of −3.4 K h^{-1} determined by Leary and Houze (1979) for tropical MCSs, but is in good agreement with the cooling rates determined for the stratiform region of the 10–11 June squall line by Willis and Heymsfield (1989) using a 1D microphysical model and with the average melting rates from the 2D retrieval (Fig. 4(b)). Uncertainties in the fall speeds, in the values of q_p and q_r, and in the depth of the melting layer, Δz, can all contribute to uncertainty in the cooling rates, so exact agreement is not expected.

* The large value and sharp decrease in fall velocity below the melting level may result partially from errors in the EVAD analysis of Rutledge *et al.* (1988a). However, the trend of decreasing fall speed with decreasing height is probably correct.

TABLE 1. PARAMETERS USED IN THE CALCULATION OF THE RATE OF COOLING BY MELTING WITHIN THE STRATIFORM PRECIPITATION REGION BASED ON EQS. (1)–(4)

	Top of melting layer	Bottom of melting layer
Height (km)	4.3	2.8
Equivalent radar-reflectivity factor for rain, Z_e (dBZ)*	27.5	35.0
Fall speed ($m\ s^{-1}$)	2.8	8.1
Mixing ratio ($g\ kg^{-1}$)	1.23	0.39
Cooling rate ($K\ h^{-1}$)	−2.7	−2.5

* The equivalent radar-reflectivity factor for ice, $dBZ_i = dBZ_e + 6.7$ dbZ.

We can compare the cooling rates estimated from the reflectivity profile with cooling rates determined from the 1D retrieval model. To do so we must specify the thermodynamic profiles for the stratiform region. Figure 11 shows the locations of rawinsondes within the composite framework of Biggerstaff and Houze (1991a) relative to the composite low-level radar-reflectivity field. Five soundings are indicated within the stratiform precipitation region; however, the sounding at RSL (Russell, KS) was taken very early (0130 UTC) and is not considered representative of the conditions within the stratiform region during the mature stage of the squall line. The soundings at PTT (Pratt, KS, at 0305 UTC), IAB (McConnell Air Force Base, KS, at 0431 UTC), and END (Enid, OK, at 0543 UTC) extended vertically to near the melting level (~600 to 630 mb) and were all very similar. The 0428 UTC END sounding extended to near 500 mb and did not appear to have been substantially modified as yet by the heavier stratiform precipitation since it was taken near the forward part of the stratiform region. Hence, it wa probably not characteristic of the conditions within the secondary maximum of rada

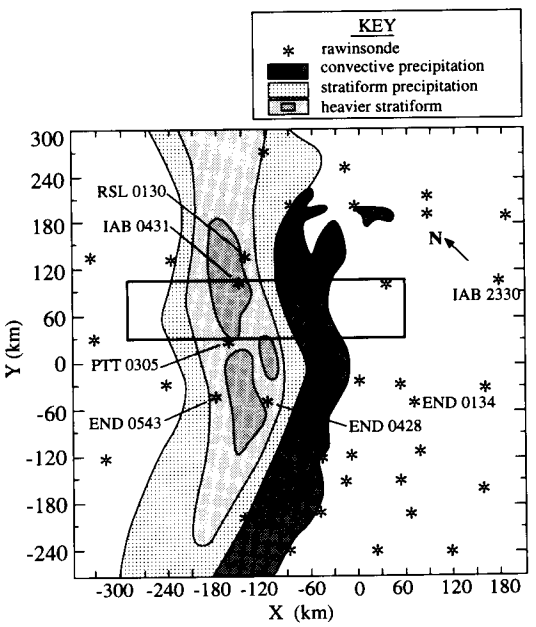

Figure 11. Map showing the 10–11 June 1985 squall line system in the composite coordinate system of Biggerstaff and Houze (1991a). The locations of the convective, stratiform, and heavier stratiform precipitation are indicated by shading. Locations of the rawinsonde soundings are indicated.

reflectivity in the stratiform region. Therefore, thermodynamic profiles below the melting level are obtained by averaging the PTT, IAB, and 0543 UTC END soundings. The 0428 UTC END sounding is used between 4.1 and 5.1 km to extend the low-level average sounding to 500 mb. These data were linearly interpolated to 100 m increments in order to resolve better the melting layer in the sounding plot (Fig. 12). For heights at and above 6.1 km (480 mb) we use the temperatures and mixing ratios from the 2D retrieval of BH1 averaged over the stratiform region ($x = -100$ to 40 km). The winds shown in the sounding (Fig. 12) are storm-relative. Winds below 5.1 km are from the average of the observed stratiform region soundings, while those at and above 6.1 km are obtained by averaging the horizontal velocities from the radar composite (Fig. 1(a)) from $x = -100$ to 40 km. Thermodynamic and velocity data at 5.6 km are obtained by averaging the values at 5.1 and 6.1 km.

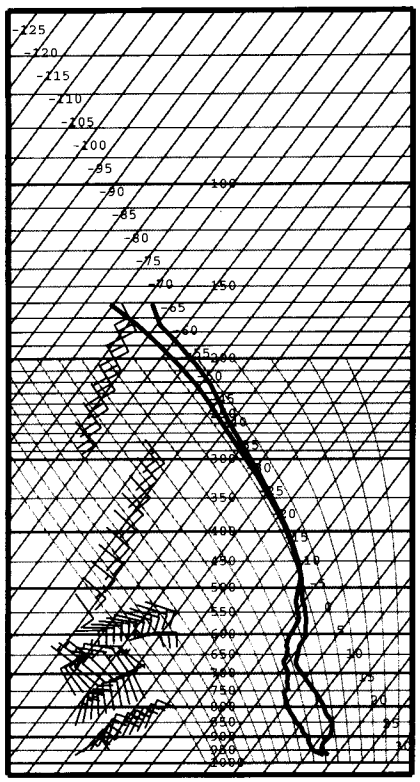

Figure 12. Stratiform region sounding obtained from low-level soundings in the stratiform region (below 500 mb) and from the thermodynamic retrieval of BH1 in the stratiform region (above 480 mb). For wind speed, one full barb = 5 m s^{-1} and one half barb = 2.5 m s^{-1}. See text for details.

The cooling by melting associated with stratiform precipitation frequently produces near 0 °C isothermal layers (Atlas *et al.* 1969; Stewart 1984; Stewart *et al.* 1984; Stewart and Macpherson 1989; Willis and Heymsfield 1989; Zhang and Gao 1989; Raga *et al.* 1991) sometimes extending through a depth of up to 1 km (Stewart 1984). Willis and Heymsfield (1989) and Zhang and Gao (1989) have shown that a near 0 °C isothermal layer, roughly 40–50 mb deep (~350 m in Willis and Heymsfield (1989) and 500 to 600 m in Zhang and Gao (1989)) occurred within the stratiform region of the 10–11 June squall

line. The 2D retrieval of BH1 was unable to reproduce such an isothermal layer. However, if we loosely define the near 0 °C isothermal layer as a layer with temperatures within the range ±0.5 °C, then the stratiform region sounding, shown in Fig. 12, contains a near 0 °C isothermal layer approximately 500 m deep between 3.8 km (643 mb) and 4.3 km (606 mb).* The depth of this layer is consistent with the mesoscale-model-derived sounding shown in Zhang and Gao (1989, see their Fig. 10(c)). Storm-relative winds show an abrupt wind shift from rear-to-front velocities below the isothermal layer to front-to-rear flow above the isothermal layer. This wind profile might suggest that the stable layer separates the rear-to-front and front-to-rear flows. However, cross-sections of dual-Doppler synthesized winds and radar reflectivities occasionally indicate that the rear-to-front jet crosses through the melting layer (across the bright band) within the stratiform region (see Rutledge *et al.* (1988a) Figs. 7 and 9, for examples).

The profiles of hydrometeor mixing ratios and melting and freezing rates obtained when using the stratiform region temperature profile are shown in Fig. 13. Maximum mixing ratios (Fig. 13(a)) of rain and precipitating ice are 0.25 and 1.1 g kg^{-1}, respectively, in general agreement with the 2D retrieval results (Fig. 2). Cloud-water is found between altitudes of 6.5 and 9.5 km and also within the melting layer. As discussed by BH1, excessive cloud-water amounts within the stratiform region can result from errors in the retrieval since cloud-water is obtained as a residual and because of the assumption that the vapour mixing ratio does not exceed its water saturation value. However, some cloud-water is expected since partially rimed ice particles were observed within the stratiform region (Rutledge *et al.* 1988b). The presence of cloud-water in the melting layer is similar to measurements in the melting layer of frontal precipitation by Stewart *et al.* (1984). The melting rate (Fig. 13(b)) peaks at -1.6 K h^{-1}, which is somewhat lower than the value obtained from the reflectivity profile (Table 1).

The time required for the cooling by melting to produce a near 0 °C isothermal layer can be estimated in a simple manner. From Atlas *et al.* (1969), the amount of heat

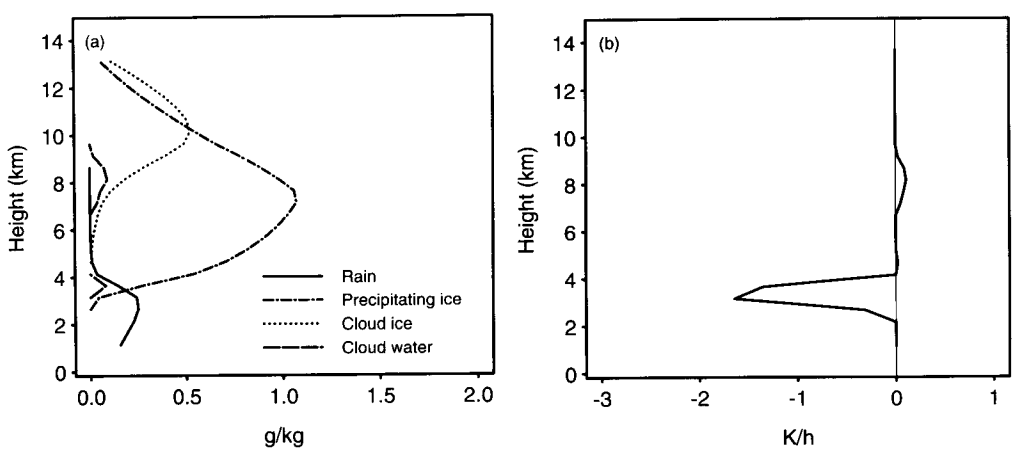

Figure 13. (a) Hydrometeor mixing-ratio profiles and (b) melting and freezing rates for the stratiform region vertical-velocity profile at 0345 UTC 11 June 1985. Freezing rates are indicated by positive values, melting rates by negative values since freezing (melting) always produces positive (negative) heating rates. Therefore, the single line shows both freezing and melting rates.

* Rutledge *et al.* (1988a) and Biggerstaff and Houze (1993) reported that the 0 °C level in the stratiform region was located near 3.8 km. As mentioned in BH1, the fall velocity cross-sections of Rutledge *et al.* (1988a) suggest a 0 °C level closer to 4.3 km. The discrepancy can be explained by the presence of the near 0 °C isothermal layer roughly between these two levels.

required to produce a 0 °C isothermal layer of depth H in a column of unit cross-sectional area with a constant initial lapse rate γ is

$$L_f m = \int_0^H \rho c_p \gamma z \, dz = \bar{\rho} c_p \gamma \frac{H^2}{2} \tag{5}$$

where m is the mass of snow melted, and $\bar{\rho}$ is the mean air density of the layer. Assuming that no other processes are acting to change the air temperature in the layer, and that the isothermal layer is produced in a time Δt, then the average rate of cooling by melting can be approximated by

$$\frac{\partial T}{\partial t} = \frac{L_f m}{c_p \bar{\rho} H \Delta t} = \frac{\gamma H}{2 \Delta t}. \tag{6}$$

Figure 14 shows the melting rate required to produce an isothermal layer of depth H in a time Δt. γ was set to 5.5 K km^{-1}, the approximate value of the moist adiabatic lapse rate near the melting level. A 500 m deep isothermal layer can be produced by a melting rate of 2 K h^{-1} within approximately 40 min. In order to estimate the residence time of an air parcel within the melting layer, consider an air parcel located initially in the middle of the secondary band and near the top of the melting layer, with a maximum storm-relative horizontal speed of 10 m s^{-1} and no vertical motion. Given that the secondary band of the 10–11 June storm had a width of approximately 100 km, the expected residence time of the air parcel in the melting layer as it moves across the secondary band is at least 1.4 h, assuming that cooling-induced downward motion does not remove the air parcel from the layer. Even if the air parcel has a mean downward velocity of 1 cm s^{-1}, it would be expected to remain in the approximately 1 km deep melting layer for about 1.4 h. Thus, neglecting other sources for temperature change, such as horizontal and vertical advection, condensation or evaporation, or heating from eddy heat fluxes, a melting rate of 2 K h^{-1} could easily produce a 500 m deep isothermal layer within the stratiform region. In fact a melting rate of 2 K h^{-1} can produce a 1 km deep isothermal layer in slightly more than one hour in the absence of other effects. However, Churchill and Houze's (1991) 2D kinematic-model calculations indicate that as the melting cools a progressively deeper layer, the lapse rate below the layer becomes unstable, leading to convective adjustment. The resultant eddy heat fluxes tend to offset some of the cooling by melting, thereby keeping in check the rate at which the near 0 °C isothermal

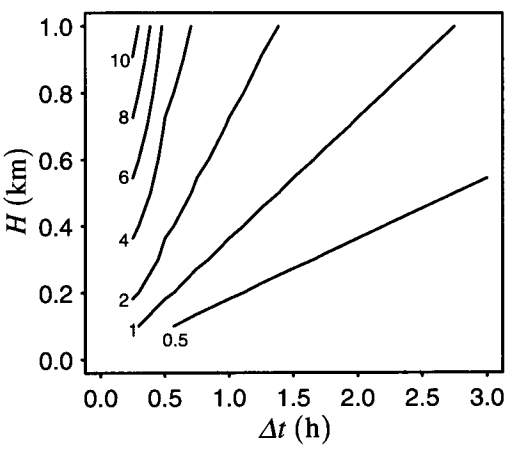

Figure 14. Melting rate (K h^{-1}) required to form a 0 °C isothermal layer of depth H in a time Δt.

layer can deepen. Condensation associated with the convective adjustment beneath the isothermal layer may also offset some of the cooling by melting.

Thermodynamic soundings at END indicate the possible effects of melting and evaporation on the low-level thermodynamic structure behind the convective line. Figure 15(a) shows the difference in potential temperature between the two END stratiform region soundings (END 0428 and END 0543, Fig. 11) and a prestorm sounding taken at END at 0134 UTC (Fig. 11), in other words, the potential-temperature perturbation from the prestorm environment. (See Fig. 3 of BH2 for a skew T–log p plot of the 0134 UTC sounding.) Perturbations below 4 km range from -4 to -11 K and show two distinct minima in both END soundings. The first minimum occurs below 1 km with peak values between -9 and -11 K, while the second minimum is located near 3.5 km, where the perturbations reach -8 K. Figure 16 shows vertical profiles of the cooling rates associated with melting of precipitating ice and evaporation of rain in both the convective (Fig. 16(a)) and stratiform regions (Fig. 16(b)). The cooling-rate profiles suggest that the low-level temperature perturbation minimum likely results from evaporation and cold surface outflow from the convective region. Cooling by melting may also be important since some of the outflow air may have originated near the melting level. On the other hand,

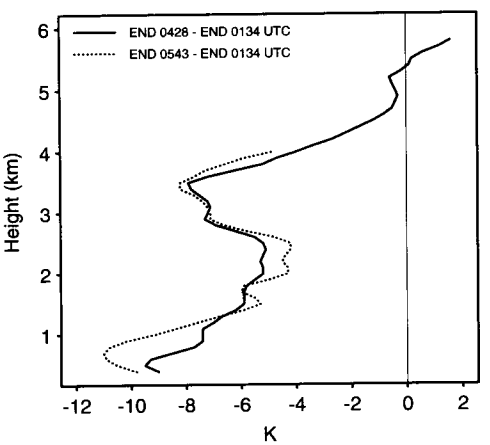

Figure 15. Potential-temperature difference between the stratiform region and the prestorm environment at END. The stratiform region soundings are for END at 0428 and 0543 UTC 11 June and the prestorm environment sounding is for END at 0134 UTC 11 June 1985.

the temperature perturbation minimum near 3.5 km is almost certainly the result of strong cooling by melting. Since the END 0428 UTC profile is located in the forward part of the stratiform region, it is uncertain whether the minimum below the melting level results from the strong melting within the convective region, or from the weaker but more widespread cooling associated with the stratiform region. In the absence of horizontal advection, one must conclude that the convective region melting must be primarily responsible for the cooling since the region of melting associated with the secondary band had not yet passed the station. However, the movement of air parcels toward the front of the squall line in the rear-to-front flow, which extends from the back edge of the storm into the convective region (Fig. 1(a)), implies that parcels may be cooled by melting within the stratiform region and then be carried into the convective region. Therefore, it is not possible at this time to identify clearly the contributions of meltin-

within the convective and stratiform regions to the observed potential-temperature perturbations immediately below the melting level.

The role of melting in the development of mesoscale and convective-scale circulations is still a matter of some debate. Chen and Cotton (1988) simulated an MCS with a 2D convective-cloud model. They found that the cold pool was about 2 °C warmer and the updraught circulations were somewhat stronger when the melting of ice was turned off. They found negligible changes in the intensity of the rear inflow and the mesoscale and convective-scale downdraughts when the cooling by melting was absent. However, the lack of melting leads to the presence of ice at warm temperatures and likely produces significant sublimation below the melting level. The added cooling associated with sublimation, as compared with the evaporation of raindrops, may compensate for the absent cooling by melting. Many other studies have indicated that melting produces mesoscale circulations, including enhanced mesoscale descent. Leary and Houze (1979) suggested that the cooling by melting in the stratiform region may be important in the initiation and maintenance of the mesoscale downdraught. Biggerstaff and Houze (1991a) found that the strongest mesoscale descent occurred in association with the enhanced (reflectivity) portions of the secondary band, where stratiform region melting would tend

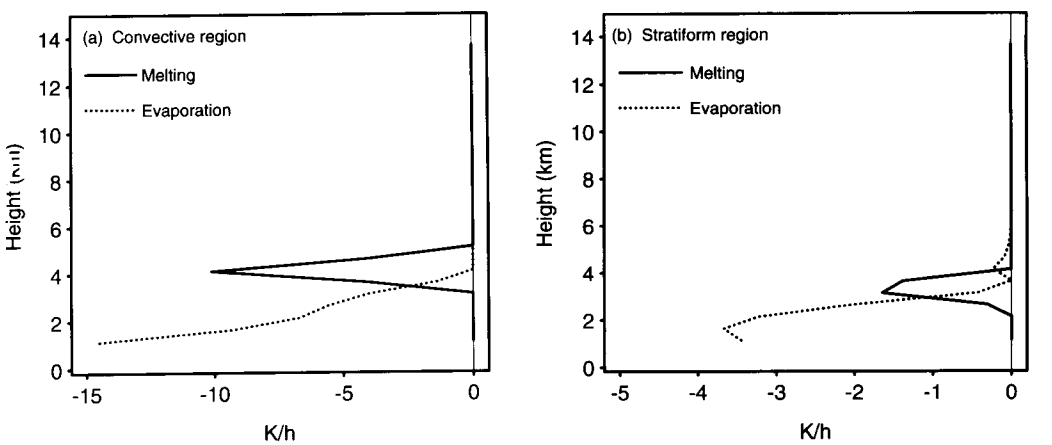

Figure 16. Vertical profiles of the cooling rates associated with melting and evaporation for (a) the convective region at 0139 UTC and (b) the stratiform region at 0345 UTC 11 June 1985.

to be strongest. Lord *et al.* (1984) noted the tendency for melting to enhance the mesoscale subsidence in a tropical cyclone. Szeto *et al.* (1988b) used a simplified 2D nonlinear numerical model to study melting-induced mesoscale circulations. For their simulation of the stratiform precipitation region of a squall line, they found that when cooling by both melting and evaporation were included, the mesoscale circulations were stronger than those that resulted from the additive effects of the individual processes. Furthermore, they suggested that melting was essential for obtaining a realistic simulation of the mesoscale circulations. When Zhang and Gao (1989) used a mesoscale model to simulate the 10–11 June 1985 squall line, they found that when the cooling by melting was turned off, the magnitudes of the mesoscale downdraught and surface pressure perturbations were significantly reduced, contrary to the simulation results of Chen and Cotton (1988). As Chen and Cotton (1988) point out, however, it is possible that the

effects of melting on mesoscale circulations may vary considerably from one convective system to the next.

5. Conclusions

Microphysical retrieval methods have been used to examine the distribution of melting and freezing within a midlatitude squall line. The 2D thermodynamic and microphysical retrieval results of BH1 were used to estimate the rates of melting and freezing within the convective and stratiform precipitation regions of the 10–11 June 1985 squall line occurring in Oklahoma and Kansas. Within the stratiform region, cooling rates associated with melting tended to be relatively uniform with magnitudes of about -2 to $-3\ \mathrm{K\ h^{-1}}$ (Figs. 3 and 4(b)), while the heating by freezing was small. In contrast, the convective region was characterized by a strong maximum in melting-induced cooling of $-14\ \mathrm{K\ h^{-1}}$ just rearward of the convective updraught and above the position of the mean convective downdraught ($x = 75$ km in Figs. 1(b) and 3). In contrast to the melting, which was contained mostly within a shallow horizontal layer, the strong heating associated with freezing was contained within a deep vertical column nearly coincident with the convective updraught, with a peak heating rate of about $8.7\ \mathrm{K\ h^{-1}}$.

The convective region was found to contribute to 56% of the total melting and 87% of the total freezing within the squall line during its mature stage. From a cloud-model simulation of the 10–11 June squall line, Tao *et al.* (1993) estimated that the convective region accounted for approximately 42% and 66%, respectively, of the total melting and freezing when averaged over the lifetime of the squall line. Their results are consistent with our findings of the strong cooling by melting occurring within the convective region.

Profiles of mean vertical velocity in the convective region were obtained from detailed dual-Doppler syntheses from the east Doppler lobe at 0139 UTC and 0209 UTC 11 June. These vertical-motion profiles were characterized by maximum mean ascent of about 2 to $2.4\ \mathrm{m\ s^{-1}}$, more than twice that of the composite data used by BH1 and BH2. Mean melting and freezing rates (Fig. 9) obtained for these profiles from the 1D retrieval reached values of -9.9 and $4.0\ \mathrm{K\ h^{-1}}$, respectively, at 0139 UTC and -10.9 and $5.3\ \mathrm{K\ h^{-1}}$ at 0209 UTC. The heating by freezing was maximum just above the freezing level (at 5.1 km), decreasing to zero near 11 km. This distribution of the heating by freezing differs substantially from that assumed by Fritsch and Chappell (1980) in their convective parametrization scheme, which has the freezing occurring at a single level, the $T = -25\ ^{\circ}\mathrm{C}$ level in their case. While the heating by freezing is generally small compared with the heating associated with condensation in convective updraughts, the magnitude and nature of the errors produced by the treatment of freezing in the Fritsch–Chappell scheme are uncertain.

We anticipate that the cooling by melting in the convective region exerts a strong influence on the development of the surface cold pool and the strength of the gust front. Srivastava (1987) and Proctor (1988) have shown that the melting of ice within downdraughts can lead to stronger descent. The positioning of the strongest melting in Fig. 3 immediately above the mean convective downdraught shown in Fig. 1(b) suggests a substantial influence of melting on the convective downdraughts. As a result, we suggest that strong melting in the convective region was important in the development of the cold pool of the 10–11 June 1985 storm.

Melting rates in the stratiform precipitation region were estimated using two methods. A melting rate of $-2.6\ \mathrm{K\ h^{-1}}$ was determined from a vertical profile of reflectivity within the stratiform region using the method outlined by Leary and Houze (1979). A comparable estimate of the melting rate from the 1D retrieval was obtained

($-1.6\,\mathrm{K\,h^{-1}}$, Fig. 13(b)). The melting in the stratiform region of the squall line produced a near 0 °C isothermal layer with a depth of approximately 500 m (Fig. 12). Using a simple formulation for the melting rate needed to produce an isothermal layer of a specified depth in a given time, we found that under ideal conditions a melting rate of $-2\,\mathrm{K\,h^{-1}}$ can produce an isothermal layer 500 m deep in about 40 min (Fig. 14), which is significantly less than the approximate residence times of air parcels within the melting layer in the secondary band. However, other processes such as condensation and eddy heat fluxes tend to offset some of the cooling by melting as the melting destabilizes the shallow layer beneath the isothermal layer, thereby limiting the rate at which the isothermal layer can deepen.

Further research is required to determine quantitatively the importance of melting and freezing on the observed storm-scale circulations. In particular, what role does melting play in the production and/or intensification of convective and mesoscale downdraughts, gust fronts, rear inflow, and frontogenesis? Is strong melting in the convective region a characteristic of most midlatitude convective systems and not of tropical systems? Studies including analysis of observations (perhaps through additional retrieval studies) as well as numerical cloud-model simulations will be needed to address these remaining issues. It is recommended that future studies that 'turn off' the melting, only remove the cooling by melting and not the process itself, since the presence of substantial amounts of ice below the melting level would likely produce significant sublimation, which may compensate for the absent cooling by melting.

Acknowledgements

We would like to thank Professor M. Biggerstaff for supplying us with the synthesized dual-Doppler radar data set used in this study and Dr Wei-Kuo Tao, Sandra Yuter, and Ming-Jen Yang for helpful comments. G. C. Gudmundson edited the manuscript and K. M. Dewar helped draft the figures. This research was sponsored by National Science Foundation grant ATM-9101653.

References

Atlas, D., Tatehira, R., Srivastava, R. C., Marker, W. and Carbone, R. E. 1969 Precipitation-induced mesoscale wind perturbations in the melting layer. *Q. J. R. Meteorol. Soc.*, **95**, 544–560

Bader, M. J., Clough, S. A. and Cox, G. P. 1987 Aircraft and dual polarization radar observations of hydrometeors in light stratiform precipitation. *Q. J. R. Meteorol. Soc.*, **113**, 491–515

Biggerstaff, M. I. and Houze Jr, R. A. 1991a Kinematic and precipitation structure of the 10–11 June 1985 squall line. *Mon. Weather Rev.*, **119**, 3034–3065

1991b Midlevel vorticity structure of the 10–11 June 1985 squall line. *Mon. Weather Rev.*, **119**, 3066–3079

1993 Kinematics and microphysics of the transition zone of the 10–11 June 1985 squall line. *J. Atmos. Sci.*, **50**, 3091–3110

Braun, S. A. and Houze Jr, R. A. 1994 The transition zone and secondary maximum of radar reflectivity behind a midlatitude squall line: Results retrieved from Doppler radar data. *J. Atmos. Sci.*, **51**, 2733–2755

1995 Diagnosis of hydrometeor profiles from area-mean vertical-velocity data. *Q. J. R. Meteorol. Soc.*, **121**, 23–53

Bringi, V., Rasmussen, R. M. and Vivekanandan, J. 1986a Multiparameter radar measurements in Colorado convective storms. Part I: Graupel melting studies. *J. Atmos. Sci.*, **43**, 2545–2563

Bringi, V., Vivekanandan, J. and Tuttle, J. D. 1986b Multiparameter radar measurements in Colorado convective storms. Part II: Hail detection studies. *J. Atmos. Sci.*, **43**, 2564–2577

Chen, S. and Cotton, W. R. 1988 The sensitivity of a simulated extratropical mesoscale convective system to longwave radiation and ice-phase microphysics. *J. Atmos. Sci.*, **45**, 3897–3910

Chong, M. and Hauser, D. 1990 A tropical squall line observed during the COPT 81 experiment in West Africa. Part III: Heat and moisture budgets. *Mon. Weather Rev.*, **118**, 1696–1706

Churchill, D. D. and Houze Jr, R. A. 1991 Effects of radiation and turbulence on the diabatic heating and water budget of the stratiform region of a tropical cloud cluster. *J. Atmos. Sci.*, **48**, 903–922

Cunning, J. B. 1986 The Oklahoma–Kansas Preliminary Regional Experiment for STORM-Central. *Bull. Am. Meteorol. Soc.*, **67**, 1478–1486

Fritsch, J. M. and Chappell, C. F. 1980 Numerical prediction of convectively driven mesoscale pressure systems. Part I: Convective parameterization. *J. Atmos. Sci.*, **37**, 1722–1733

Fulton, R. and Heymsfield, G. M. 1991 Microphysical and radiative characteristics of convective clouds during COHMEX. *J. Appl. Meteorol.*, **30**, 98–116

Gallus Jr, W. A. and Johnson, R. H. 1991 Heat and moisture budgets of an intense midlatitude squall line. *J. Atmos. Sci.*, **48**, 122–146

Hallett, J., Sax, R. I., Lamb, D. and Ramachandra Murty, A. S. 1978 Aircraft measurements of ice in Florida cumuli. *Q. J. R. Meteorol. Soc.*, **104**, 631–652

Houze Jr, R. A. 1982 Cloud clusters and large-scale vertical motions in the tropics. *J. Meteorol. Soc. Japan*, **60**, 396–410

1989 Observed structure of mesoscale convective systems and implications for large-scale heating. *Q. J. R. Meteorol. Soc.*, **115**, 425–461

1993 *Cloud dynamics*. Academic Press, San Diego

Houze Jr, R. A., Smull, B. F. and Dodge, P. 1990 Mesoscale organization of springtime rainstorms in Oklahoma. *Mon. Weather Rev.*, **118**, 613–654

Illingworth, A. J., Goddard, J. W. F. and Cherry, S. M. 1987 Polarization radar studies of precipitation development in convective storms. *Q. J. R. Meteorol. Soc.*, **113**, 469–489

Johnson, R. H. and Hamilton, P. J. 1988 The relationship of surface pressure features to the precipitation and airflow structure of an intense midlatitude squall line. *Mon. Weather Rev.*, **116**, 1444–1472

Koenig, L. R. 1963 The glaciating behavior of small cumulonimbus clouds. *J. Atmos. Sci.*, **20**, 29–47

Knupp, K. R. 1987 Downdrafts within High Plains cumulonimbi. Part I: General kinematic structure. *J. Atmos. Sci.*, **44**, 987–1008

1988 Downdrafts within High Plains cumulonimbi. Part II: Dynamics and thermodynamics. *J. Atmos. Sci.*, **45**, 3965–3982

Kuo, Y.-H. and Anthes, R. A. 1984 Mesoscale budgets of heat and moisture in a convective system over the central United States. *Mon. Weather Rev.*, **112**, 1482–1497

Leary, C. A. and Houze Jr, R. A. 1979 Melting and evaporation of hydrometeors in precipitation from anvil clouds of deep tropical convection. *J. Atmos. Sci.*, **36**, 669–679

Lin, X. and Johnson, R. H. 1994 Heat and moisture budgets and circulation characteristics of a frontal squall line. *J. Atmos. Sci.*, **51**, 1661–1681

Lord, S. J., Willoughby, H. E. and Piotrowicz, J. M. 1984 Role of parameterized ice-phase microphysics in an axisymmetric, nonhydrostatic tropical cyclone model. *J. Atmos. Sci.*, **41**, 2836–2848

Meischner, P. F., Bringi, V. N., Heimann, D. and Höeller, H. 1991 A squall line in southern Germany: Kinematics and precipitation formation as deduced by advanced polarimetric and Doppler radar measurements. *Mon. Weather Rev.*, **119**, 678–701

Proctor, F. H. 1988 Numerical simulations of an isolated microburst. Part I: Dynamics and structure. *J. Atmos. Sci.*, **45**, 3137–3160

Raga, G. B., Stewart, R. E. and Donaldson, N. R. 1991 Microphysical characteristics through the melting region of a midlatitude winter storm. *J. Atmos. Sci.*, **48**, 843–855

Rutledge, S. A., Houze Jr, R. A., Biggerstaff, M. I. and Matejka, T. 1988a The Oklahoma–Kansas mesoscale convective system of 10–11 June 1985: Precipitation structure and single-Doppler radar analysis. *Mon. Weather Rev.*, **116**, 1409–1430

Rutledge, S. A., Houze Jr, R. A., Heymsfield, A. J. and Biggerstaff, M. I. 1988b 'Dual-Doppler and airborne microphysical observations in the stratiform region of the 10–11 June MCS over Kansas during PRE-STORM'. Pp. 705–707 in Preprints, Tenth International Cloud Physics Conference, Offenbach am Main. Deutscher Wetterdienst

Smull, B. F. and Houze Jr, R. A. 1987 Rear inflow in squall lines with trailing stratiform precipitation. *Mon. Weather Rev.*, **115,** 2869–2889

Srivastava, R. C. 1987 A model of intense downdrafts driven by the melting and evaporation of precipitation. *J. Atmos. Sci.*, **44,** 1752–1773

Srivastava, R. C., Matejka, T. J. and Lorello, T. J. 1986 Doppler-radar study of the trailing anvil region associated with a squall line. *J. Atmos. Sci.*, **43,** 356–377

Stewart, R. E. 1984 Deep 0 °C isothermal layers within precipitation bands over southern Ontario. *J. Geophys. Res.*, **89**(D2), 2567–2572

Stewart, R. E. and Macpherson, S. R. 1989 Winter storm structure and melting-induced circulations. *Atmos.–Ocean*, **27,** 5–23

Stewart, R. E., Marwitz, J. D., Pace, J. C. and Carbone, R. E. 1984 Characteristics through the melting layer of stratiform clouds. *J. Atmos. Sci.*, **41,** 3227–3237

Szeto, K. K., Lin, C. A. and Stewart, R. E. 1988a Mesoscale circulations forced by melting snow. Part I: Basic simulations and dynamics. *J. Atmos. Sci.*, **45,** 1629–1641

Szeto, K. K., Stewart, R. E. and Lin, C. A. 1988b Mesoscale circulations forced by melting snow. Part II: Application to meteorological features. *J. Atmos. Sci.*, **45,** 1642–1650

Tao, W.-K., Simpson, J., Sui, C.-H., Ferrier, B., Lang, S., Scala, J., Chou, M.-D. and Pickering, K. 1993 Heating, moisture, and water budgets of tropical and mid-latitude squall lines: Comparisons and sensitivity to long-wave radiation. *J. Atmos. Sci.*, **50,** 673–690

Vivekanandan, J., Bringi, V. and Raghavan, R. 1990 Multiparameter radar modeling and observations of melting ice. *J. Atmos. Sci.*, **47,** 549–564

Wakimoto, R. M. and Bringi, V. N. 1988 Dual-polarization observations of microbursts associated with intense convection: The 20 July storm during the MIST project. *Mon. Weather Rev.*, **116,** 1521–1539

Waldvogel, A., Klein, L., Musil, D. J. and Smith, P. L. 1987 Characteristics of radar-identified big drop zones in Swiss hail-storms. *J. Climate Appl. Meteorol.*, **26,** 861–877

Willis, P. T. and Heymsfield, A. J. 1989 Structure of the melting layer in mesoscale convective system stratiform precipitation. *J. Atmos. Sci.*, **46,** 2008–2025

Yanai, M., Esbensen, S. and Chu, J. H. 1973 Determination of bulk properties of tropical cloud clusters from large-scale heat and moisture budgets. *J. Atmos. Sci.*, **30,** 611–627

Yuter, S. and Houze Jr, R. A. 1994 Three-dimensional kinematic and microphysical evolution of Florida cumulonimbus, Part II: Frequency distributions of vertical velocity, reflectivity, and differential reflectivity. *Mon. Weather Rev.*, in press

Zhang, D.-L. and Gao, K. 1989 Numerical simulation of an intense squall line during 10–11 June 1985 PRE-STORM. Part II: Rear inflow, surface pressure perturbations, and stratiform precipitation. *Mon. Weather Rev.*, **117,** 2067–2094